Force-momentum fields in a dual-jet flow

By DAVID R. MILLER* AND EDWARD W. COMINGS†
Purdue University, Lafayette, Indiana

(Received 17 April 1959)

Measurements of mean velocity, mean flow direction, normal turbulent stress in the direction of flow, and mean static pressure are reported for the subsonic flow field generated by identical twin jets of air issuing from parallel slot nozzles in a common wall and mixing turbulently with ambient room air. At the low nozzle velocity employed (72 ft./sec), the two-dimensional plano-symmetric flow was effectively incompressible. Since the end walls prevented interjet air entrainment from the surroundings, a region of highly convergent flow was formed near the nozzles. In this region, contour maps clearly reveal (1) the sub-atmospheric static pressure trough that accounts for the jet convergence, (2) a free stagnation point on the plane of symmetry, (3) stable symmetrical contrarotary vortices which recycle air on the concave side of each converging jet, and (4) the super-atmospheric static pressure mound that redirects the merging jet streams in a common downstream direction. Comparisons are made between the development of the flow, in both the region of jet convergence and the region of combined jet flow, and that of the single-jet counterpart which was previously reported.

1. Introduction

In an earlier paper by the present authors (Miller & Comings 1957), measurements of the force-momentum fields in a two-dimensional incompressible free air jet were reported. Particular emphasis was placed on the role of the mean static pressure stresses in the Reynolds equations of motion. It was shown that the pressure stresses and stress gradients are of the same order of magnitude as the normal turbulent stresses $\rho\overline{u'^2}$ and $\rho\overline{v'^2}$ and their gradients, but of opposite sign. As consequences of this near cancellation of stresses in the region of turbulence, the deceleration of the mean flow along a streamline depends almost entirely on the lateral gradient of turbulent shear stress τ, and mean flow accelerations lateral to a streamline are quite small, i.e. the streamlines are nearly straight. In this paper a jet flow is considered in which static pressure effects are far more pronounced in accelerating the mean flow both along and across the streamlines.

The two-dimensional flow in question is that produced by the subsonic flow of air from twin nozzles set in a common end wall, as illustrated in figure 1. All solid boundaries, shown in cross-section, extend sufficiently far in the z-direction to ensure two-dimensionality at the plane ($z = 0$) depicted in the figure. In addition, the extension of the end wall (the plane $x = 0$) in the y-directions is effectively

* Now at Research and Engineering Division, Monsanto Chemical Company, Dayton, Ohio.
† Now at University of Delaware, Newark.

infinite. The centre-plane ($y = 0$) is the plane of symmetry for both flow and boundaries.

Practically no information on dual-jet flows is available in the literature. Corrsin (1944) investigated the unstable flow from seven parallel slot nozzles in a common wall, with emphasis on flow stabilization methods. His nozzles had a width of only 0·20 in., but were geometrically similar to the nozzles of this study. Temperature, total head, and flow directions were reported. Bollinger (1950) measured mean velocity traverses in the combined flow region of twin round jets set with their axes at various angles to each other with the flows converging. The

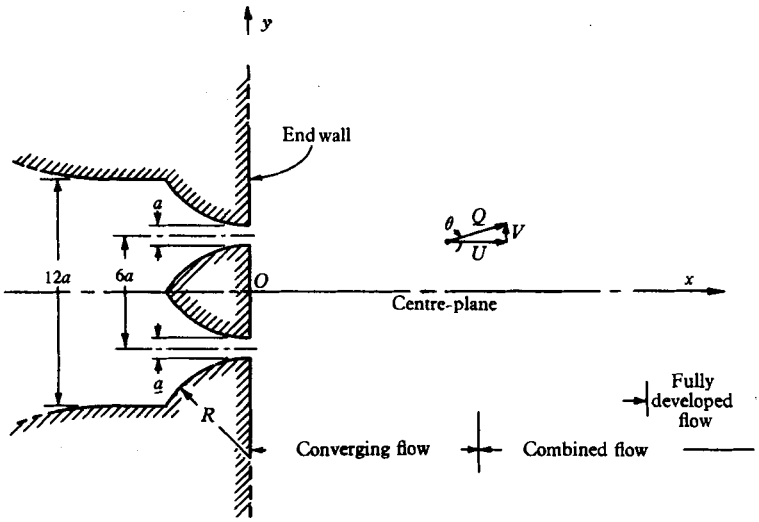

FIGURE 1. Nozzle and flow geometry in the plane $z = 0$. $a = 0{\cdot}500$ in., $R = 2{\cdot}617$ in.

momentum flux distribution in the combined flow region differed greatly from the distribution calculated by adding the momentum flux from the separate jets at the same point in space. Considerable curvature of the streamlines was indicated. Laurence & Benninghoff (1957) have reported extensive mean velocity and turbulence measurements in the fields of multiple interfering air jets produced by several multiple nozzle configurations. In all cases studied, however, the jets were allowed to mix freely with ambient air, and static pressure effects were consequently minimized.

Despite the paucity of previous data, the major features of the dual-jet flow may be inferred *a priori* from the behaviour of simpler turbulent jets and wakes. Thus one would expect to find a region of pronounced negative gauge static pressure $\overline{p}$ between the jets near the end wall, due to the pumping effect of turbulent momentum transfer from the individual jets to the central region. Consequences of the negative pressure are converging curvature of the individual jets and non-conservation of x-momentum. As the two jets are about to merge, one would expect static pressure gradients to be largely responsible for redirecting their momenta in the x-direction and for reversing that portion of the flow earlier entrained on the concave sides of the jets. After the jets have merged, the resultant single-jet flow can be expected to resemble a classical single-jet flow,

the similarity becoming more marked with downstream distance. A downstream transition from large to small static pressure gradients serves to delineate a boundary between the converging and combined flow regions as illustrated in figure 1. As might be expected, the mean x-velocity (U) profile achieves full development a short distance downstream from this boundary.

2. Equations of motion

Under the restrictions placed on the dual-jet flow (and its single-jet counterpart), the appropriate equations of motion in customary Cartesian notation, using Cartesian co-ordinates, are

$$\text{(Continuity)} \qquad \frac{\partial U}{\partial x}+\frac{\partial V}{\partial y}=0, \tag{1}$$

$$(x\text{-Reynolds}) \qquad \frac{\partial}{\partial x}(\rho U^2+\rho\overline{u'^2}+\overline{p})+\frac{\partial}{\partial y}(\rho UV-\tau+\mu\zeta)=0, \tag{2}$$

$$(y\text{-Reynolds}) \qquad \frac{\partial}{\partial y}(\rho V^2+\rho\overline{v'^2}+\overline{p})+\frac{\partial}{\partial x}(\rho UV-\tau-\mu\zeta)=0, \tag{3}$$

where $\tau=-\rho\overline{u'v'}$ is the turbulent shear stress and $\zeta=\partial V/\partial x-\partial U/\partial y$ is the mean vorticity. The mean x- and y-components of velocity U and V define a vector field identically described by two new scalar field variables—Q, the vector magnitude, and θ, the vector angle measured counter-clockwise from the positive x-axis. While these variables, defined in (7), are hereafter called the mean velocity and flow direction, they are not generally identical to the mean magnitude and mean direction of the instantaneous velocity vector.

At any point in the flow, the above equations of motion may be transformed to a local co-ordinate system aligned with the flow by a rotation of the (x, y)-axes through the angle θ. In the local co-ordinate system, s measures distance in the direction of flow and m (rotated y-axis) measures distance perpendicular to s. The transformed equations are

$$\text{(Continuity)} \qquad \frac{\partial Q}{\partial s}+Q\frac{\partial\theta}{\partial m}=0, \tag{4}$$

$$(s\text{-Reynolds}) \qquad \frac{\partial}{\partial s}(\tfrac{1}{2}\rho Q^2+\rho\overline{u_s'^2}+\overline{p})-\frac{\partial}{\partial m}(\tau_s-\mu\zeta)=0, \tag{5}$$

$$(m\text{-Reynolds}) \qquad \kappa\rho Q^2+\frac{\partial}{\partial m}(\rho\overline{v_s'^2}+\overline{p})-\frac{\partial}{\partial s}(\tau_s+\mu\zeta)=0. \tag{6}$$

The subscript s on the turbulent stresses indicates that they are the (s, m) components of the turbulent stress tensor; and $\kappa=\partial\theta/\partial s$ is recognized as the local streamline curvature. Several of the important transform relations are

$$Q\cos\theta=U, \quad Q\sin\theta=V, \tag{7}$$

$$\rho\overline{u_s'^2}=\rho\overline{u'^2}\cos^2\theta-2\tau\cos\theta\sin\theta+\rho\overline{v'^2}\sin^2\theta, \tag{8}$$

$$\rho\overline{v_s'^2}=\rho\overline{u'^2}\sin^2\theta+2\tau\cos\theta\sin\theta+\rho\overline{v'^2}\cos^2\theta, \tag{9}$$

$$\tau_s=\tau(\cos^2\theta-\sin^2\theta)+(\rho\overline{u'^2}-\rho\overline{v'^2})\cos\theta\sin\theta, \tag{10}$$

$$\zeta=\kappa Q-\frac{\partial Q}{\partial m}=\frac{\partial V}{\partial x}-\frac{\partial U}{\partial y}. \tag{11}$$

Equations (4), (5) and (6) apply to the entire flow field when s and m are interpreted as distances along the orthogonal curvilinear co-ordinates formed by the streamlines and their orthogonals. We now define the stream function ψ which satisfies (1) and is zero on the plane of symmetry:

$$\psi = \int_0 U\,dy = \int_0 Q\cos\theta\,dy. \tag{12}$$

Streamline slope and curvature are now given by the relations

$$dy_\psi/dx = \tan\theta, \quad \kappa = d\theta_\psi/ds = \partial\theta/\partial s. \tag{13}$$

The use of curvilinear co-ordinates in analysing the flow in the converging region of the dual jet simplifies comparisons with the single-jet flow. In the single jet, the mid-nozzle streamline is a straight line coinciding with the x-axis: in the dual jet, each mid-nozzle streamline is highly curved until the individual jets have merged into a single jet. In comparisons based on the mid-nozzle streamlines, s is equivalent to x in the single jet. A new straight-line co-ordinate n, perpendicular to the mid-nozzle streamline and tangential to the local curvilinear m-co-ordinate, is equivalent to y in the single jet.

In the jet flows under consideration, all flow variables except the stream function must approach zero as y approaches $\pm\infty$. This fact, with the conditions of symmetry of the variables, leads to the total mass and momentum integrals from (1) and (2):

$$\rho\int_0^\infty U\,dy = \rho\psi_\infty \quad \text{(a constant)}, \tag{14}$$

$$\int_0^\infty (\rho U^2 + \rho\overline{u'^2} + \overline{p})\,dy = J \quad \text{(a constant)}. \tag{15}$$

A convenient definition of the jet width b is

$$b(x) = \int_0^\infty (U/U_c)^2\,dy, \tag{16}$$

where U_c is the centre-plane ($y = 0$) value of U at the x-station of the integration.

3. Apparatus

But for the removal of a dummy converging wall originally blocking flow from one of the twin nozzles, the flow equipment was identical to that described in the earlier paper. A low-speed wind tunnel provided a uniform low-turbulent horizontal flow of room air to the dual nozzles of aspect ratio 40:1 depicted in horizontal section in figure 1. The nominal nozzle velocity U_r was 72 ft./sec, corresponding to a nozzle Reynolds number aU_r/ν of $1{\cdot}78\times10^4$. Ceiling and floor boundaries over and under the jet flow helped maintain the two-dimensional character of the flow while permitting free horizontal mixing of the jets with ambient air.

Mean and fluctuating velocities were measured with a constant temperature hot-wire anemometer similar to one described by Laurence & Landes (1952). The single tungsten wire, of 0·0002 in. diameter and 0·080 in. active length, was supported vertically in the flow, i.e. parallel to the z-axis. Measurements of mean

static pressure were obtained with a static pressure probe of the disk type and connecting Prandtl micromanometer. These same two instruments were employed in the single-jet study; a more detailed description appears in the earlier paper.

Two instrument probes were used in measuring and indicating local flow direction. The first was a rotatable impact tube supported vertically in the flow. A side impact opening, of 0·021 in. diameter, was located near the upper sealed end of the tube, which was of 0·065 in. outside diameter and 2·5 in. length. The lower end of the tube formed the journal of a fine half-bearing machined in the end of the horizontal supporting member; it also carried a 0·5 in. diameter coaxial sheave for angular control, and provided a pressure connexion via small bore rubber tubing with the micromanometer. A remote graduated hand dial and spring loaded piano wire loop communicated known angular settings to the impact tube. In use, the direction of maximum indicated pressure was taken as the average of two angles of equal indicated pressure straddling the peak angle.

The second flow-direction probe consisted of a light aluminum foil vane, of 1·5 in. vertical length and 0·2 in. width, attached along its vertical leading edge to a wire spindle carried in the conical end bearings of a fork support. No provision was made or needed for accurate vane-angle measurement, since this probe was primarily used in regions of high streamline curvature where positional accuracy is more important than angular accuracy.

Measuring probes were individually positioned in the (x, y)-plane, midway between the ceiling and floor boundaries, with a precision of several thousandths of an inch by means of a lead-screw traversing mechanism. A detailed description of apparatus and procedures is available (Miller 1957).

4. Interpretation of measurements

Some uncertainty is inevitable in the interpretation of 'point' measurements obtained in turbulent flows. Townsend (1956) notes that such measurements commonly concern those quantities that are easy to measure rather than those which have an easily understood significance. Two reasons may be cited: (1) the 'easily understood' quantities are abstractions of a type precluding *direct* measurement by present techniques, and (2) no existing measuring process is so perfectly understood and so free of indeterminate influences as to permit an assumption-free definitive formulation of its cause-to-effect relation. The confidence placed in a given interpretation, therefore, can only be justified by incomplete circumstantial evidence; examples are incomplete theory, comparisons between different instruments, and findings of internal or external consistencies. A brief discussion of interpretation practices employed in this investigation follows.

Hot-wire measurements

The single hot-wire and associated constant-temperature anemometer circuits produces a voltage e assumed to be uniquely and instantaneously related (through steady flow calibration) to the magnitude q of the velocity vector

perpendicular to the wire. When the fluctuation of q, i.e. q', is small relative to its mean $\bar{q}$, then

$$f(\bar{e}) = \bar{q} = Q \quad \text{and} \quad \overline{e'^2}\left[\frac{df(\bar{e})}{de}\right]^2 = \overline{q'^2} = \overline{u_s'^2},$$

where f represents the functional e *vs* q relation obtained by calibration. Measurements of $\bar{e}$ and the mean square of e' were converted to Q and the mean square of u_s' by means of these relations. In flow regions of high turbulence intensity, the above expressions no longer hold. At a point where Q is actually zero (for example, at the free stagnation point and the vortex centre),

$$f(\bar{e}) \doteqdot \bar{q} = \sqrt{(\overline{u_s'^2} + \overline{v_s'^2})} > Q,$$

and

$$\overline{e'^2}\left[\frac{df(\bar{e})}{de}\right]^2 \doteqdot q'^2 = \overline{u_s'^2} + \overline{v_s'^2} - \bar{q}^2 \doteqdot \overline{u_s'^2}.$$

These approximate equalities recognize the non-linearity of f at low q (a linearizing circuit was not employed). Q values are readily corrected in the neighbourhood

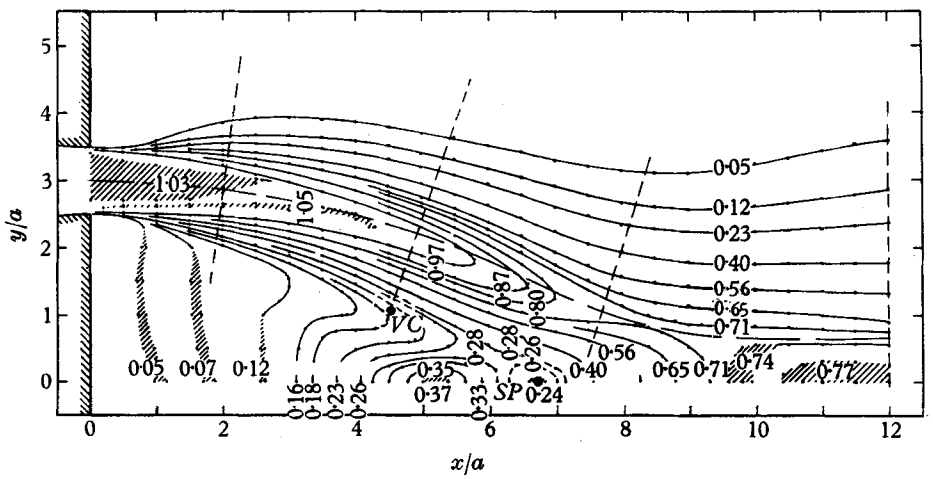

FIGURE 2. Mean velocity contours. Shaded areas are regions of constant velocity within the accuracy of hot-wire measurements. The points marked *VC* and *SP* are respectively the vortex centre and free stagnation point. The mid-nozzle streamline ($\psi = 0{\cdot}48$) starting at $x = 0$, $y = 3a$ is shown, as well as the paths of the four lateral traverses whose profiles are given in figures 5 to 8. Values of Q/U_r.

of singular points by interpolation from surrounding regions of low turbulence intensity, using the location of the point fixed by vane-probe measurements. The method is illustrated in the U/U_r profile of figure 10. All computations involving Q, e.g. the streamline mapping of figure 3, incorporated this method of correction. For purposes of discussion, the Q contours of figure 2 were not corrected. Turning to the fluctuation term $\overline{u_s'^2}$, no correction could be applied since no independent estimate of $\overline{v_s'^2}$ was available. Reported values of this variable are subject to considerable error within a radius of $\frac{1}{2}a$ of the two singular points.

Flow direction

The impact direction probe gave measures of the direction of maximum impact pressure as contrasted to the flow angle θ previously defined. As is demonstrated in figure 3, the two quantities may differ by as much as 40° in a turbulent jet flow, where strong lateral gradients of velocity and static pressure exist. Most of this error was removed by a method of streamline plotting. This method, discussed in

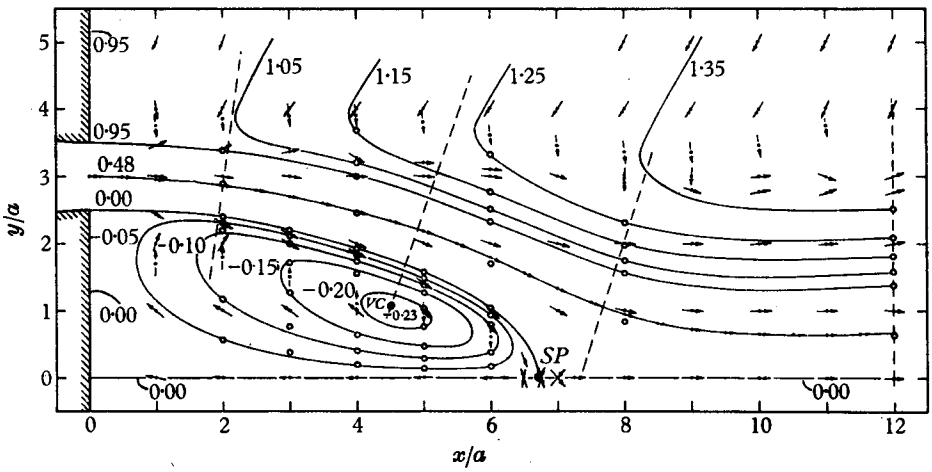

FIGURE 3. Mean flow directions and streamlines determined from the impact probes (solid arrows) and the vane (broken arrows). Values of ψ/aU_r.

conjunction with figure 3, depends strongly on the corrected Q-field and is relatively insensitive to impact direction measurements. It is justified by the excellent agreement found between the path of the mid-nozzle streamline so determined and the path established from impact direction measurements alone. Vane directions agreed everywhere with the calculated streamline directions, within the ability of the eye to judge.

Static pressure

Theory is of no assistance in evaluating the reliability of the static pressure measurements, since the external and internal aerodynamics of the probe and connecting passage are too complex and obscure. Confidence is instead based on the internal and external consistency of the single-jet static pressure measurements, as presented in the earlier paper. There is as yet no indication of significant bias in the measurements, in either the single- or dual-jet flows. Hinze (1959) discusses static pressure measurements at some length.

5. Results—converging region ($0 < x/a < 12$)

Complete tables and graphs of experimental data are available elsewhere (Miller 1957). Measurements revealed, as expected, a high degree of flow symmetry about the centre-plane; consequently, data taken only in the positive y half-plane are reported. At $x/a = 12$, the initially individual jets had merged

and the flow variables resembled those in a single-jet flow. This was consequently selected to be the downstream limit of the converging region and the beginning of the combined flow region.

Mean velocity field

Figure 2 is a contour map of the mean velocity or Q-field. Contour levels were arbitrarily selected to give adequate coverage; and points corresponding to a single level were located by traversing the probe through the flow. The value of each level was then determined from hot-wire traverses carried out after the contours were plotted. To facilitate comparisons with other figures, the positions of several characteristic lines and points are indicated in the figure. The reference velocity U_r, previously referred to as the nominal nozzle velocity, is defined as that hypothetical nozzle velocity whose kinetic pressure $\frac{1}{2}\rho U_r^2$ is equal to the measured gauge impact pressure at the centre of the nozzle mouth. This particular definition, selected for convenience in hot-wire calibration and data reduction, does not require that $Q/U_r = 1{\cdot}00$ at the centre of the nozzle mouth.

Flow direction and streamline fields

Mean flow directions and streamlines appear in figure 3. Solid and broken arrows represent flow directions measured with the impact and vane direction probes, respectively. The vortex centre and free stagnation point were found using the vane probe. At the free stagnation point the vane whipped around in all directions at random without favouring any one; at the vortex centre the vane rotated rapidly and continuously. Detection of the two points by the vane method was found to be remarkably sensitive and reproducible; no two measurements of their positions differed by more than $0{\cdot}132a$ or 0·066 in. in either co-ordinate. Crossed arrows in the vicinity of the free stagnation point reflect the fact that two symmetric pressure maxima were found on rotating the impact direction probe about its axis.

The mid-nozzle streamline $\psi/aU_r = 0{\cdot}48$ was established from impact direction measurements exclusively. Using the velocity contours of figure 2, an original estimate of its path was made. The impact direction probe was then traversed along the estimated path with readings of θ taken at $\frac{1}{2}$ in. intervals. These readings were used in a numerical integration of the first relation of (13) to obtain an improved estimate of the path. Three repetitions of this iterative procedure (the last with an x-interval of 0·25 in.) gave satisfactory convergence. Analysis of the final curve yielded its curvature κ from (13) and arc length s as functions of x. All other streamlines were calculated from (12) using the measured flow directions and Q-values from figure 2. Calculated points are indicated by circles in figure 3. In the vicinity of the two nozzle lip streamlines near the nozzle, the agreement between streamline and measured flow directions is poor. This is a result of the gradient error of the impact direction probe discussed earlier. In these regions, the streamlines are more accurate indicators of true flow directions.

Among the features revealed in figure 3 are: (1) one of the two contrarotary stable vortices which recycles air (24 % of that issuing from the nozzles) between the jets, (2) the stagnation of the streamline from the inner lip of the nozzle at

SP, and (3) curvature, spread, and confluence of the jets. Air entrained on the outer side of the jet is seen to approach at an angle near 245°. The corresponding streamlines, if sufficiently extended, would reveal another large vortex system outside the jet in accordance with the requirement of (14).

Static pressure field

Mean static pressure contours appear in figure 4. Comparisons with the previous contour maps give an immediate qualitative picture of the important role of static pressure gradients in accelerating the mean flow, particularly in regard to

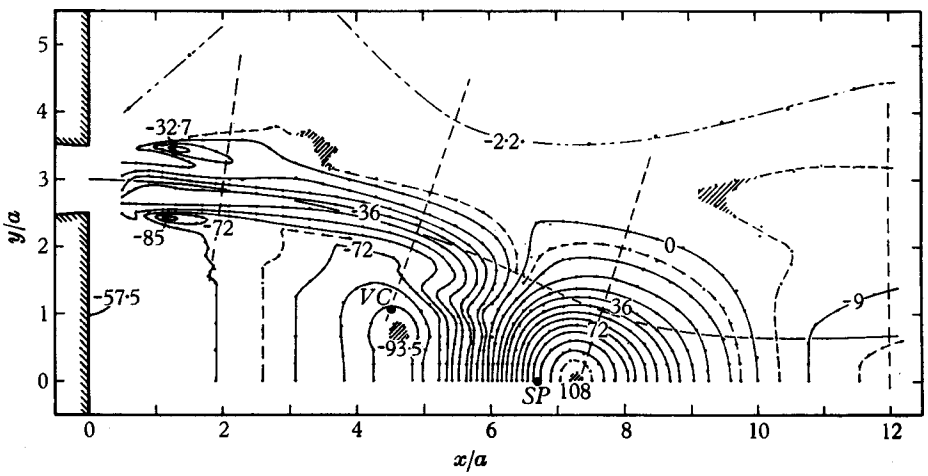

FIGURE 4. Mean static pressure contours. Values of $\bar{p}/\rho U_r^2 \times 10^3$. —, contour interval = 9; – – –, mid-contour.

lateral acceleration resulting in streamline curvature. Except in the static pressure mound between $x/a = 6$ and $x/a = 10$, all regions of the flow were at less than atmospheric pressure (negative $\bar{p}$). The static pressure mound around $x/a = 7$, whose peak is near the free stagnation point, is largely responsible for the stagnation and for the reversal of the flow between jets. Downstream from the mound a return to the modest static pressure gradients typical of a single free jet is observed.

Lateral traverses

Further aspects of the converging flow are best revealed in profile diagrams derived from probe traverses indicated in figures 2–4. Proceeding downstream along the mid-nozzle streamline, the four lateral traverses perpendicular to the streamline and intersecting it at $s/a = 2$, 5, 8, 12·4 correspond to the profiles of figures 5–8 respectively. Traverse measurements included mean velocity Q, turbulent s-stress $\rho\overline{u_s'^2}$, and mean static pressure $\bar{p}$.

The mean velocity profiles of figures 5–7 are fairly symmetrical about $n = 0$ and similar in shape (but not of equal peak height) to single-jet profiles taken at equal distances from the nozzle. A comparison of the widths of the velocity profiles at various downstream distances in table 1 reveals practically identical spreading tendencies in the converging jet and the single free jet out to 8 nozzle-slit widths

from the nozzle. Beyond $8a$ the comparison breaks down due to the confluence of the converging jets in the dual-jet flow. In table 1 jet width is taken to be the lateral distance between the two profile points where the mean velocity is half of

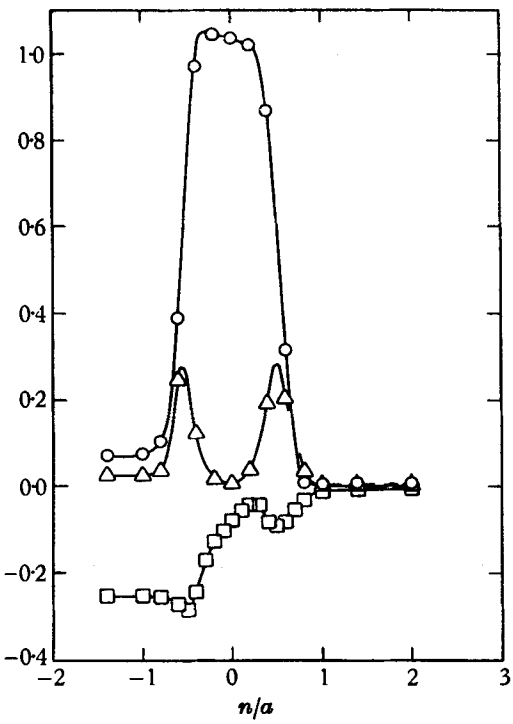

FIGURE 5. Lateral traverse at a distance $s/a = 2$ measured downstream from the nozzle along the mid-nozzle streamline. Circles, triangles and squares refer respectively to mean velocity Q, turbulent stress $\rho\overline{u_s'^2}$, and mean static pressure $\bar{p}$. ○, Q/U_r; △, $10\overline{u_s'^2}/U_r^2$; □, $4\bar{p}/\rho U_r^2$.

	Half velocity jet width / Nozzle width (a)	
x/a or s/a	Dual jet	Single jet
2	1·06	1·14
3	(1·15)	1·20
4	(1·24)	1·26
5	1·33	—
6	(1·46)	1·50
8	1·96	—
10	—	2·24

TABLE 1. Comparison of dual- and single-jet widths near nozzles.

the profile peak value. Numbers in parentheses were obtained from figure 2 and are less accurate than the others. Consequences of the nearly equal profile spreading are developed later in the discussion of the mid-nozzle streamline profiles.

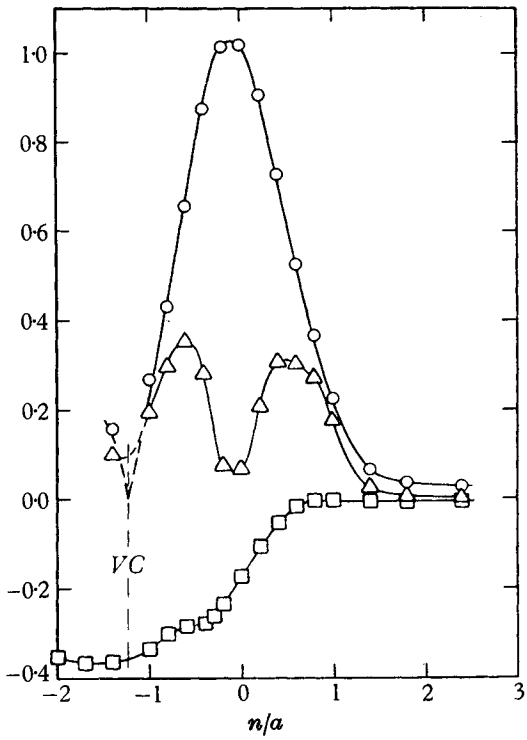

FIGURE 6. Lateral traverses at $s/a = 5$. ○, Q/U_r; △, $10\overline{u_s'^2}/U_r^2$; □, $4\overline{p}/\rho U_r^2$.

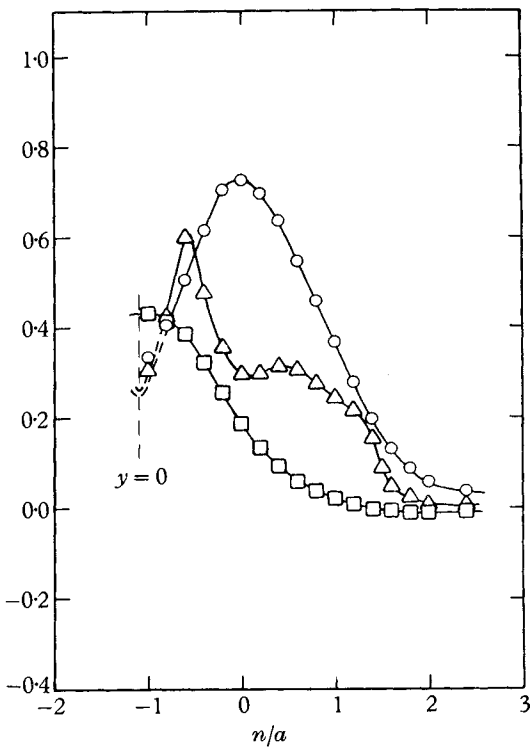

FIGURE 7. Lateral traverses at $s/a = 8$. ○, Q/U_r; △, $10\overline{u_s'^2}/U_r^2$; □, $4\overline{p}/\rho U_r^2$.

Turning to the turbulent stress profiles of figures 5–8, several interesting features are observed in the downstream development of the two-peaked curve when compared to its single-jet counterpart. (In the single-jet flow, of course, the peaks are symmetrical about the x-axis.) Starting near $s/a = 5$, the inner stress peak (negative n) begins a period of rapid growth relative to the outer peak (positive n),

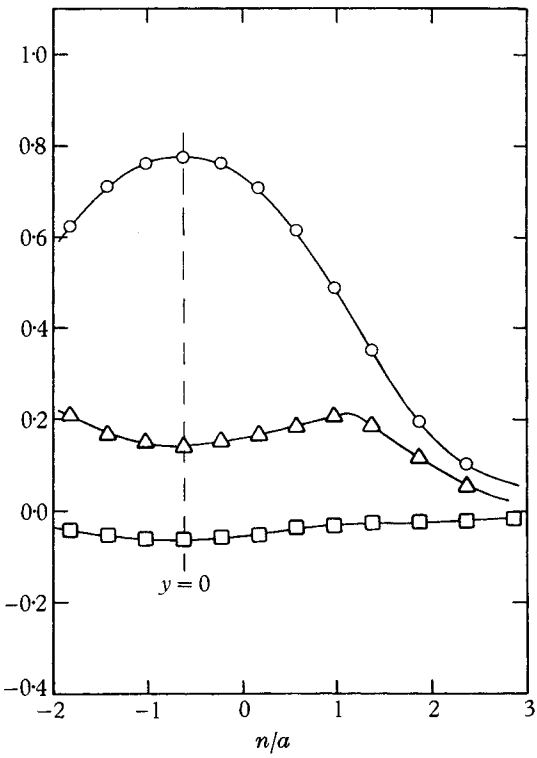

FIGURE 8. Lateral traverses at $s/a = 12{\cdot}4$. ○, Q/U_r; △, $10\overline{u_s'^2}/U_r^2$; □, $4\overline{p}/\rho U_r^2$.

whereas the outer peak spreads more rapidly and develops a hump clearly evident at $s/a = 8$. Downstream from $s/a = 8$, in the region where the two jets intermingle, the inner stress peak decays quite rapidly; at $s/a = 12{\cdot}4$ no trace of an inner peak remains. The limited turbulence measurements reported here preclude a coherent discussion of the reasons for the observed behaviour of the stress profile; it can only be stated that moderate differences exist in the production, transport, and dissipation of turbulence energy between the inner and outer shear regions of the converging jet and either shear region of the single jet.

Static pressure profiles of figures 5–7 bear no resemblance to corresponding single-jet profiles. In the discussion of figure 4, mention was made of the role of static pressure in curving the streamlines. To explore this further, we rearrange (6) in the form

$$\kappa\rho Q^2 + \frac{\partial \overline{p}}{\partial m} = \frac{\partial}{\partial s}(\tau_s + \mu\zeta) - \frac{\partial}{\partial m}(\rho\overline{v_s'^2}), \tag{17}$$

and hypothesize that the right-hand side is zero along the mid-nozzle streamline of the converging jet. Note that in the single jet along the centre-plane each term

of (17) is exactly zero, due to the symmetry of the flow. To test the hypothesis, values of the two left-hand terms were calculated at various points along the mid-nozzle streamline. Resulting values in dimensionless form are listed in table 2. These results show that the lateral static pressure gradient at the mid-nozzle streamline was at least the dominant force causing streamline curvature. That better agreement was not obtained is ascribed more to the diversity of measurement errors involved (velocity, flow direction, static pressure) than to the influence of any term on the right-hand side of (17).

s/a	$\kappa a Q^2/U_\tau^2$	$\partial(\overline{p}/\rho U_\tau^2)/\partial(m/a)$
2	−0·064	0·055
3·5	−0·076	0·090
5	−0·076	0·081
6·5	−0·011	0·011
6·63	0·000	0·000
8	0·088	−0·097
9·5	0·049	−0·023

TABLE 2. Lateral accelerations and static pressure gradients on the mid-nozzle streamline.

Analyses similar to the above have been carried out in other regions of the flow. The general conclusion is that both turbulent stress gradients and static pressure gradients contribute to lateral flow acceleration; the latter dominates where Q is large and κ is small (as along the mid-nozzle streamline), and the former dominates where Q is small and κ is large (as in the regions of entrainment).

Longitudinal traverses

Profiles of Q, $\overline{u_s'^2}$, and $\overline{p}$, obtained by traverse measurements along the mid-nozzle streamline and along the centre-plane, appear in figures 9 and 10, respectively. Considering the former first, the effect of the static pressure gradient along the streamline on the mean velocity is evident. In particular, the static pressure peak near $x/a = 8$ is largely responsible for the dip in the mean velocity decay curve. The turbulent stress profile contains a peak, also near $x/a = 8$, which is sharper and 45 % higher than the corresponding peak in the single-jet flow.

Neglecting the viscous stress term, the Reynolds equation (5) respective to the s-direction is

$$\frac{\partial}{\partial s}\left(\tfrac{1}{2}\rho Q^2 + \rho\overline{u_s'^2} + \overline{p}\right) - \frac{\partial \tau_s}{\partial m} = 0. \tag{18}$$

The quantity in parentheses was computed at various stations along the mid-nozzle streamline for both the converging and single jets. Results are compared in table 3. Good agreement indicates that the distribution of the turbulent shear stress τ_s about the mid-nozzle streamline was practically identical in the two flows despite differences in the mean velocity levels. Equal spreading of the two jet flows, discussed in conjunction with table 1, further establishes the similarity of the turbulent shear stress fields in the cores of the jets.

Turning to the centre-plane profiles of figure 10, note the (x, y)-co-ordinates and components are used because of the coincidence of the traverse with the x-axis.

Plotting U instead of Q reveals more clearly the reversal of the mean flow and the nature of the previously mentioned error in mean velocity measurement near the free stagnation point. The data of this figure were analysed in a manner similar

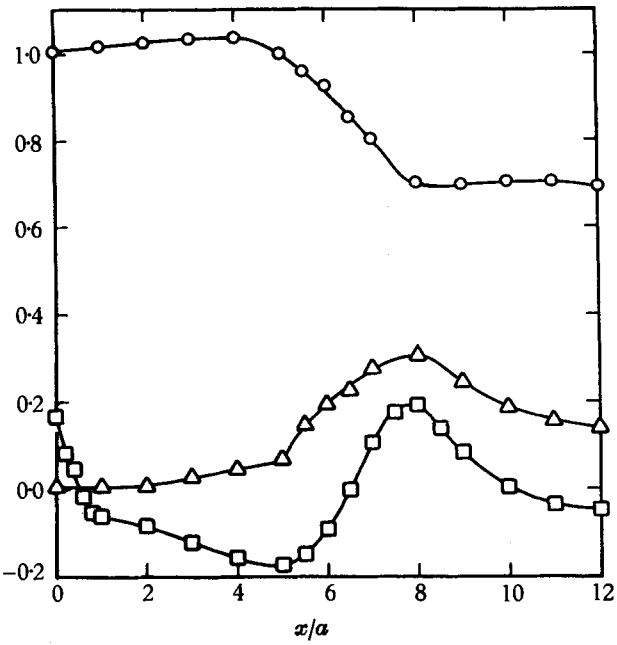

FIGURE 9. Longitudinal tranverses along the mid-nozzle streamline.
○, Q/U_r; △, $10\overline{u_s'^2}/U_r^2$; □, $4\overline{p}/\rho U_r^2$.

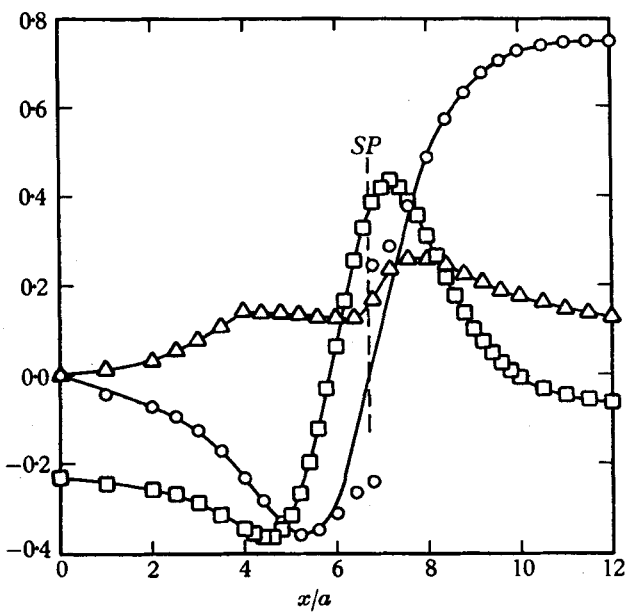

FIGURE 10. Longitudinal traverses along the central plane.
○, U/U_r; △, $10\overline{u'^2}/U_r^2$; □, $4\overline{p}/\rho U_r^2$.

to that of the preceding figure. Equation (18) when written for the centre-plane streamline is

$$\frac{\partial}{\partial x}(\tfrac{1}{2}\rho U^2+\rho\overline{u'^2}+\overline{p})-\frac{\partial \tau}{\partial y}=0. \tag{19}$$

Again the quantity in parentheses was computed at a number of stations along the centre-plane. A plot of these data against x yielded a smoothed curve remarkably symmetrical about $x/a = 6{\cdot}57$ (very near the free stagnation point) and quite well represented by a Gaussian error integral curve as follows:

$$(\tfrac{1}{2}\rho U^2+\rho\overline{u'^2}+\overline{p})/\rho U_r^2 = 0{\cdot}337\int_{-\infty}^{w}\Phi(w')\,dw'-0{\cdot}059, \tag{20}$$

where $$\Phi(w')=\frac{1}{\sqrt{(2\pi)}}\exp(-\tfrac{1}{2}w'^2), \quad w=0{\cdot}658(x/a-6{\cdot}57).$$

	$\dfrac{\rho Q^2+2\rho\overline{u_s'^2}+2\overline{p}}{\rho U_r^2}$	
s/a, x/a	Dual jet	Single jet
4	1·00	1·01
6	0·86	0·87
8	0·69	0·70
10	0·55	0·57
12	0·49	0·49

TABLE 3. Comparison of mid-nozzle streamline decay.

Differentiating (20) with respect to x/a gives the turbulent shear stress gradient,

$$\frac{\partial}{\partial(y/a)}\left(\frac{\tau}{\rho U_r^2}\right)=0{\cdot}089\exp[-0{\cdot}216(x/a-6{\cdot}57)^2], \tag{21}$$

which is a Gaussian error curve centred at $x/a = 6{\cdot}57$ with a peak value of 0·089. These relations hold in the range $0 < x/a < 11$. In view of flow symmetry, τ itself is zero along the centre-plane.

From the foregoing it is apparent that the turbulent shear stress gradient tends to accelerate the mean flow in the positive x-direction at all points along the centre-plane out to $x/a = 11$; the maximum tendency occurs very near the free stagnation point. Alternately reinforcing and opposing this tendency is the effect due to the static pressure gradient along the x-axis. In the range $4{\cdot}5 < x/a < 7{\cdot}2$, the static pressure gradient tends to accelerate the flow in the negative x-direction against the influence of the turbulent shear stress. Flow stagnation occurs at the point (SP) where the two forces are equal and opposite. The x-gradient of the normal turbulent stress $\rho\overline{u'^2}$ in (19) was generally negligible in comparison to the static pressure and turbulent shear stress forces.

6. Results—combined jet region ($x/a > 12$)

On merging, the converging jets of the dual-jet flow lose their individual identities and behave as a single jet. The analysis of the flow in the combined jet region is therefore identical to that of the previously reported single-jet flow

(Miller & Comings 1957). Indeed, the combined jet flow is so nearly similar to the single-jet flow that it will suffice to describe the similarities and differences without repeating the more detailed development of the earlier paper.

Mean velocity and jet width

A fully developed turbulent jet is characterized by (1) linear spread with downstream distance, (2) power-law decay of the centre-plane mean velocity with downstream distance, and (3) similarity of the lateral mean velocity profile. These three properties are expressed in the relations

$$b/a = c(x/a - x_0/a), \tag{22}$$

$$U_c^2/U_r^2 = K(x/a - x_0/a)^{-C}, \tag{23}$$

$$U/U_c = f(\eta), \quad \text{where} \quad \eta = y/b. \tag{24}$$

In these equations c, x_0, K and C are experimental constants, b is the jet width (a function of x) defined in (16), and U_c is the centre-plane mean velocity at a given value of x. Certain restrictions are imposed on the values of the experimental constants by the condition of momentum conservation expressed in (15). These restrictions, listed in the last lines of table 4 together with values of the various experimentally determined quantities, are necessarily approximate since momentum alone is not strictly conserved, even in the single jet.

Factor	Combined dual jet	Single jet
Region of fully developed flow		
$x/a >$	23	7
c	0·072	0·0723
x_0/a	−5·50	−1·572
K	11·1	6·74
C	1·03	1·028
$f(\eta)$	$\exp(-\frac{1}{8}\pi\eta^2)$	$\exp(-\frac{1}{8}\pi\eta^2)$
Restrictions		
$C \doteqdot$	1·0	1·0
$cK \doteqdot J/\rho U_r^2 =$	0·86	0·48

TABLE 4. Comparison of mean velocity properties in the fully developed jet.

The data of table 4 with equations (22), (23) and (24) give a complete description of the mean velocity fields of the two flows after the mean velocity profiles achieved similarity. The station where this occurred, listed on the first line, was considerably farther from the nozzle in the dual-jet case because of the extended region of convergence of the individual jets. Rates of spread and decay of the profiles were identical in the two flows as indicated by the equality of c and C in each case. Also identical were the dimensionless analytic functions $f(\eta)$ best fitting the experimental data. The only marked differences found were in the position of the 'virtual origin' x_0 and in the value of the velocity level constant K.

All comparisons thus far made can be summarized in a single statement as follows: if the two nozzles of the dual-jet flow were replaced by a single nozzle of the same size as either, located on the centre-plane at $x/a = -3{\cdot}93$ and having

a nozzle mouth velocity 1·29 times that of the original dual nozzles, then the mean velocity field at $x/a > 23$ would be indistinguishable in all respects from the original field.

Dimensionless mean velocity profiles appear in figure 11. It is noted that the data have not been corrected to remove the slight influence of the lateral velocity V on the hot-wire in the region $2{\cdot}5 < \eta < 4{\cdot}0$. The smooth curve through the points obtained at $x/a = 20$, 30, 40 is identical to the best curve through the uncorrected data of the single jet. Points of the $x/a = 12$ profile do not conform to the curve since the flow had not reached full development at that station.

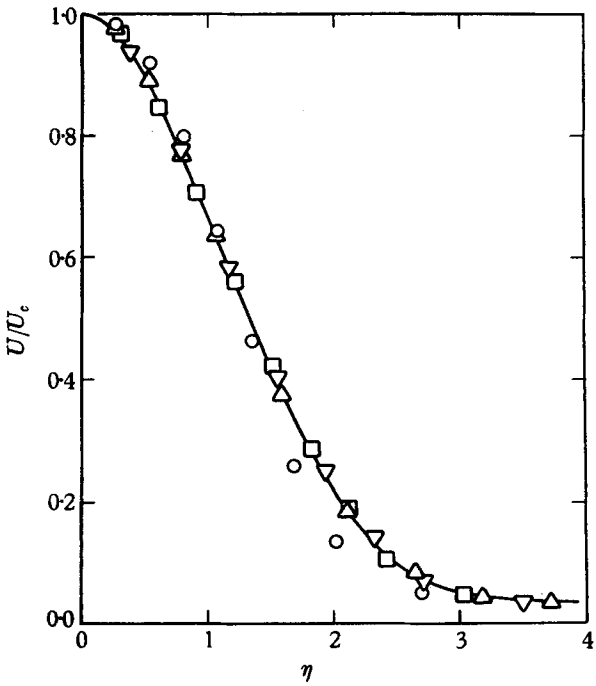

FIGURE 11. Mean velocity profiles for $x/a \geqslant 12$. ○, 12; △, 20; ▽, 30 and □, 40. The solid curve is identical with that obtained for a single jet.

Turbulent x-stress and static pressure profiles

As should be expected, the downstream development of the turbulent x-stress and static pressure profiles resembles that of the single-jet flow. The turbulent stress profiles of figure 12 exhibit 'partial self-preservation' at $x/a = 20$, 30 and 40, as evidenced by a coincidence of the curves at large η and an apparent tendency to converge on a single fully self-preserving curve as x approaches infinity. A convergence of the static pressure profiles on a self-preserving form is apparent in figure 13. With the exception of the turbulent stress profile at $x/a = 12$, all of the curves are typical in shape and height to those obtained in a single-jet flow. This, however, is as far as the similarities go. No simple equivalence was found in the distance histories of the profiles. This is shown in the data of table 5, which lists the approximate downstream station of the single-jet flow at which the given dual-jet profile was most nearly duplicated. These data reveal a near-normal

development of the static pressure field, accompanied by an initially retarded but rapid development of the x-stress field. Finally, at $x/a = 40$, the x-stress profile is 'in step' with the static pressure profile; both are nearly identical to the corresponding single-jet profiles at $x/a = 35$.

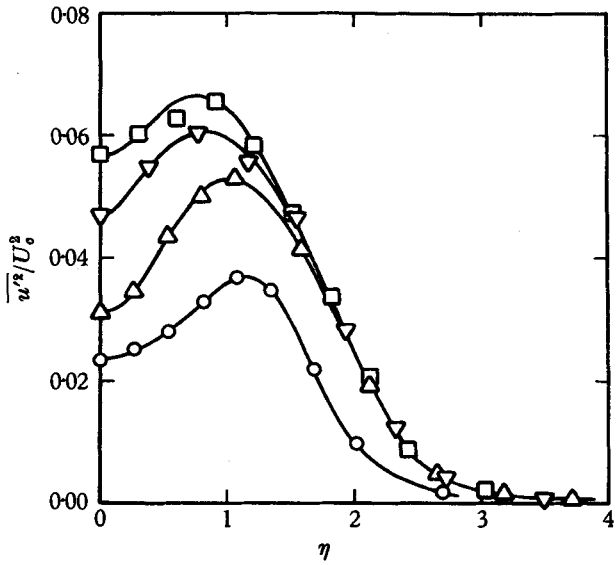

FIGURE 12. Turbulent x-stress profiles. $x/a \geqslant 12$: ○, 12; △, 20; ▽, 30; □, 40.

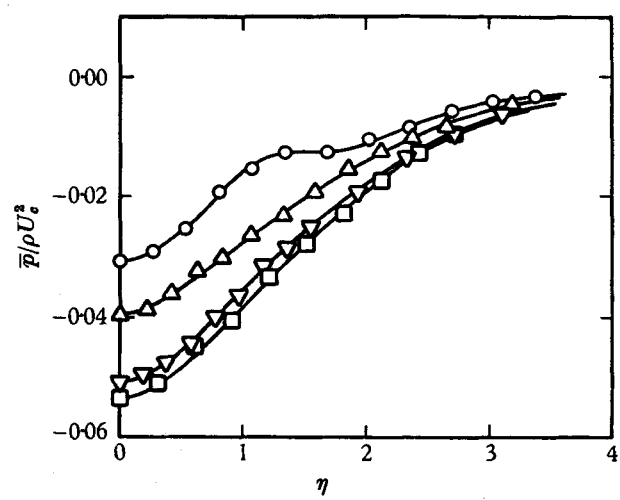

FIGURE 13. Static pressure profiles. $x/a \geqslant 12$: ○, 12; △, 20; ▽, 30; □, 40.

Thus so far no mention has been made of the nature of the turbulent y-stress $\rho\overline{v'^2}$ and shear stress τ fields. In the earlier paper it was shown that in the fully developed single jet (1) dimensionless y-stress profiles are nearly identical to coincident static pressure profiles with the sign inverted, and (2) the shear stress profile reaches full self-preservation at the same station as the mean velocity profile does. We also note that the turbulent x- and y-stresses are identical to twice the

x- and y-components of the energy of turbulence. These facts taken all together give some insight into the precedence of approach to self-preservation (or dynamic equilibrium) of the turbulent motion and energy in the combined jet region. First to reach full self-preservation is the turbulent shear stress at $x/a = 23$. The turbulent y-stress or y-energy distribution quickly assumes a characteristic single-jet form and approximate growth rate downstream from the region of convergence. Lagging behind but rapidly catching up to single-jet proportions is the x-stress or x-energy. It is assumed, but without supporting evidence, that the dual-jet flow downstream from $x/a \doteqdot 40$ would have been found to be completely indistinguishable from a single-jet flow originating in a suitably placed single nozzle.

Dual-jet profile station, x/a	Equivalent single-jet profile station, x/a	
	Turbulent x-stress	Static pressure
12	None	13
20	8	20
30	22	32
40	35	34

TABLE 5. Profile equivalence.

7. Conclusions

Based on the experimental data presented and on the results of a previous investigation of a single free jet, a reasonably clear description of the mean and turbulent motion in a two-dimensional dual-jet flow is possible. In the region of jet convergence near the nozzles, the structure of the flow in the core of either jet is quite similar to that of a single free jet provided due account is taken of the mean flow accelerations attributable to a radically different static pressure field. A region of sub-atmospheric static pressure between the converging jets accounts for their convergence and for the reversal of a considerable fraction of the total flow at the centre-plane against a strong downstream force of turbulent shear. Associated with the flow reversal is the appearance of a pair of symmetrical contrarotary stable vortices and a free stagnation point on the centre-plane. Where the two jets merge, a super-atmospheric static pressure mound redirects their momenta into a single resultant jet symmetrical about the centre-plane. The flow structure of the combined jet exhibits all characteristics of a single-jet flow except for an altered evolution of the turbulence toward self-preservation. This is ascribed to differences in upstream conditions.

For valuable assistance in the course of this work, the authors are indebted to Professor Sydney Goldstein of Harvard University and Mr James C. Laurence of the N.A.S.A. Lewis Research Center. Financial support was generously provided by The Barrett Division, Allied Chemical and Dye Corporation, and by the Purdue Research Foundation.

REFERENCES

BOLLINGER, E. H. 1950 M.S. Thesis, University of Illinois.

CORRSIN, S. 1944 *Nat. Adv. Comm. Aero., Wash., Wartime Rep.* no. W-90.

HINZE, J. O. 1959 *Turbulence.* New York: McGraw-Hill.

LAURENCE, J. C. & BENNINGHOFF, J. M. 1957 *Nat. Adv. Comm. Aero., Wash., Tech. Note* no. 4029.

LAURENCE, J. C. & LANDES, L. G. 1952 *Nat. Adv. Comm. Aero., Wash., Tech. Note* no. 2843.

MILLER, D. R. 1957 Ph.D. Dissertation, Purdue University.

MILLER, D. R. & COMINGS, E. W. 1957 *J. Fluid Mech.* **3**, 1–16.

TOWNSEND, A. A. 1956 *The Structure of Turbulent Shear Flow.* Cambridge University Press.